Monthly Notices of the ROYAL ASTRONOMICAL SOCIETY

MNRAS **534,** 3552–3564 (2024) https://doi.org/10.1093/mnras/stae2300
Advance Access publication 2024 October 7

JWST/NIRSpec spectroscopy of intermediate-mass quiescent galaxies at $z \sim 3$–4

Riku A. Sato,[1★] Akio K. Inoue,[1,2] Yuichi Harikane,[3] Rhythm Shimakawa,[4,5] Yuma Sugahara,[1,2,6] Yoichi Tamura,[7] Takuya Hashimoto,[8,9] Kei Ito,[10] Satoshi Yamanaka,[11] Ken Mawatari,[2] Yoshinobu Fudamoto[12] and Yi W. Ren[1]

[1]*Department of Pure and Applied Physics, Graduate School of Advanced Science and Engineering, Faculty of Science and Engineering, Waseda University, 3-4-1 Okubo, Shinjuku, Tokyo 169-8555, Japan*
[2]*Waseda Research Institute of Science and Engineering, Faculty of Science and Engineering, Waseda University, 3-4-1 Okubo, Shinjuku, Tokyo 169-8555, Japan*
[3]*Institute for Cosmic Ray Research, The University of Tokyo, 5-1-5 Kashiwanoha, Kashiwa, Chiba 277-8582, Japan*
[4]*Waseda Institute for Advanced Study (WIAS), Waseda University, 1-21-1 Nishi-Waseda, Shinjuku, Tokyo 169-0051, Japan*
[5]*Center for Data Science, Waseda University, 1-6-1 Nishi-Waseda, Shinjuku, Tokyo 169-0051, Japan*
[6]*National Astronomical Observatory of Japan, 2-21-1 Osawa, Mitaka, Tokyo 181-8588, Japan*
[7]*Department of Physics, Graduate School of Science, Nagoya University, Furo, Chikusa, Nagoya, Aichi 464-8602, Japan*
[8]*Division of Physics, Faculty of Pure and Applied Sciences, University of Tsukuba, Tsukuba, Ibaraki 305-8571, Japan*
[9]*Tomonaga Center for the History of the Universe (TCHoU), Faculty of Pure and Applied Sciences, University of Tsukuba, Tsukuba, Ibaraki 305-8571, Japan*
[10]*Department of Astronomy, Graduate School of Science, The University of Tokyo, 7-3-1 Hongo, Bunkyo-ku, Tokyo 113-0033, Japan*
[11]*General Education Department, National Institute of Technology, Toba College, 1-1 Ikegami-cho, Toba, Mie 517-8501, Japan*
[12]*Center for Frontier Science, Chiba University, 1-33 Yayoi-cho, Inage-ku, Chiba 263-8522, Japan*

Accepted 2024 October 2. Received 2024 September 30; in original form 2024 February 19

ABSTRACT

We present the analysis of three intermediate-mass quiescent galaxies (QGs) with stellar masses of $\sim 10^{10}\,M_\odot$ at redshifts $z \sim 3$–4 using NIRSpec low-resolution spectroscopy. Utilizing the spectral energy distribution fitting code BAGPIPES, we confirm these target galaxies are consistent with quiescent population, with their specific star formation rates falling below 2 dex the star-forming main sequence at the same redshifts. Additionally, we identify these QGs to be less massive than those discovered in previous works, particularly prior to the *JWST* era. Two of our target galaxies exhibit the potentially blended Hα + [N II] emission line within their spectra with signal-to-noise ratio >5. We discuss whether this feature comes from an active galactic nucleus (AGN) or star formation, although future high-resolution spectroscopy is required to reach a conclusion. One of the target galaxies is covered by *JWST*/NIRCam imaging of the Public Release IMaging for Extragalactic Research survey. Using the 2D profile fitting code GALFIT, we examine its morphology, revealing a disc-like profile with a Sérsic index of $n = 1.1 \pm 0.1$. On the size–mass relation, we find a potential distinction between less massive ($\log_{10}(M_*/M_\odot) < 10.3$) and massive ($\log_{10}(M_*/M_\odot) > 10.3$) QGs in their evolutionary pathways. The derived quenching time-scales for our targets are less than 1 Gyr. This may result from these galaxies being quenched by AGN feedback, supporting the AGN scenario of the emission line features.

Key words: galaxies: evolution – galaxies: high-redshift.

1 INTRODUCTION

Quiescent galaxies (QGs) are passively evolving galaxies that do not display significant star formation activity when compared to the star-forming main sequence (SFMS; see e.g. Brinchmann et al. 2004; Whitaker et al. 2012, 2014; Speagle et al. 2014; Santini et al. 2017; Houston, Croton & Sinha 2023; Popesso et al. 2023). Previous research has sought to understand the processes through which these galaxies cease their star formation activities. The cessation of star formation is commonly referred to as 'quenching' in the context of galaxy evolution. The high-redshift quiescent population is regarded as the progenitors of local massive early-type galaxies (ETGs). Studying high-redshift QGs is crucial for understanding the formation of galaxies across cosmic time.

For years, several quenching mechanisms, such as feedback of active galactic nuclei (AGNs) or star formation (e.g. Croton et al. 2006; Maiolino et al. 2012; Peng, Maiolino & Cochrane 2015; Zolotov et al. 2015; Piotrowska et al. 2022; Bluck et al. 2024), environmental quenching including ram pressure stripping (e.g. Boselli, Fossati & Sun 2022), and morphological quenching (e.g. Martig et al. 2009) have been considered to explain the quenching mechanism (e.g. Gabor et al. 2010; Peng et al. 2010b; Somerville & Davé 2015; Zolotov et al. 2015; Bluck et al. 2024).

The size–mass relation, which is between the effective radius and stellar mass of galaxies, is important for understanding how galaxies

★ E-mail: sato.riku2019@toki.waseda.jp

© 2024 The Author(s).
Published by Oxford University Press on behalf of Royal Astronomical Society. This is an Open Access article distributed under the terms of the Creative Commons Attribution License (https://creativecommons.org/licenses/by/4.0/), which permits unrestricted reuse, distribution, and reproduction in any medium, provided the original work is properly cited.

Downloaded from https://academic.oup.com/mnras/article/534/4/3552/7815198 by guest on 18 April 2025

are formed and evolved across cosmic time. QGs are more compact than star-forming galaxies (SFGs), and have larger sizes with larger stellar mass (e.g. van der Wel et al. 2014; Nedkova et al. 2021). The size–mass relation for QGs has a steeper slope compared to that for SFGs (e.g. van der Wel et al. 2014; Nedkova et al. 2021). In the context of the size evolution of QGs (e.g. van der Wel et al. 2014; Nedkova et al. 2021), minor mergers are believed to play a dominant role, as supported by past observations (e.g. Bezanson et al. 2009; Newman et al. 2012; van der Wel et al. 2014) and simulations (e.g. Naab, Johansson & Ostriker 2009). These minor mergers contribute to the steeper size–mass relation observed for QGs (e.g. Ownsworth et al. 2014; van Dokkum et al. 2015). Some studies show the flattening of size–mass relation at the low-mass end (e.g. Kawinwanichakij et al. 2021; Nedkova et al. 2021). The size evolution of galaxies might not be driven by mergers but rather by star formation at low-mass end (e.g. van Dokkum et al. 2015; Cutler et al. 2024).

QGs in the high-z Universe are intrinsically so faint that it is challenging to detect them. Previously, near-infrared (NIR) instruments on ground-based telescopes made the advancement of spectroscopic confirmation of QGs at $z > 3$ (Glazebrook et al. 2017; Schreiber et al. 2018a,b; Tanaka et al. 2019; Forrest et al. 2020; Valentino et al. 2020; D'Eugenio et al. 2021; Antwi-Danso et al. 2023; Kakimoto et al. 2024). However, these QGs were found to be massive galaxies with a stellar mass of $\log_{10}(M_*/\mathrm{M}_\odot) > 10.3$. Photometric candidates at $z > 3$ with stellar masses $\gtrsim 10^9\,\mathrm{M}_\odot$ were also reported before *JWST* era (e.g. Mawatari et al. 2016, 2020; Davidzon et al. 2017; Merlin et al. 2019; Santini et al. 2019), but it is important to emphasize that these were not spectroscopically confirmed. The *JWST*, with its remarkable sensitivity in the NIR, has enabled the detection of these high-redshift, less massive QGs, opening a new era of QG research. In recent studies, less massive and/or high-redshift ($z \gtrsim 3$) QGs have been detected using *JWST*, photometrically (Alberts et al. 2023; Carnall et al. 2023a; Valentino et al. 2023; Cutler et al. 2024) and spectroscopically (Carnall et al. 2023b, 2024; Marchesini et al. 2023; Sandles et al. 2023; Strait et al. 2023; de Graaff et al. 2024; Looser et al. 2024; Nanayakkara et al. 2024; Weibel et al. 2024).

Here we report three QGs at $z \simeq 3$–4 observed by using *JWST* Near-Infrared Spectrograph (NIRSpec). We analyse the obtained low-resolution ($R \sim 100$) spectroscopic data. Our samples are less massive galaxies with the stellar masses of $\log_{10}(M_*/\mathrm{M}_\odot) < 10.3$ estimated from spectral fitting. Two of our samples, HD1 and HD3, show line emission feature considered as the Hα + [N II] emission line. Additionally, HD3 has *JWST* Near-Infrared Camera (NIRCam) and *JWST* Mid-Infrared Instrument (MIRI) imaging data, allowing us to study the morphology of the low-mass QG.

This paper is structured as follows. In Section 2, we detail the data employed in this study. In Section 3, we explain our analysis methods and the results. In Section 4, we discuss about formation and evolution of QGs based on our results. Section 5 offers a summary of our findings. In this paper, we adopt a standard set of the cosmological parameters of $(\Omega_\mathrm{m}, \Omega_\Lambda, h) = (0.3, 0.7, 0.7)$.

2 DATA

2.1 Target galaxies

Target galaxies, named HD1, HD2, and HD3, have been identified as H-band dropout galaxies in the wide and deep imaging data set in the Cosmological Evolution Survey (COSMOS; Scoville et al. 2007) and Subaru/*XMM–Newton* Deep Survey Field (SXDF; Furusawa et al. 2008) fields collected by using ground-based telescopes and *Spitzer* (Harikane et al. 2022). Harikane et al. (2022) employed $grizy$ images from the Hyper Suprime-Cam Subaru Strategic Program (HSC-SSP) survey (Aihara et al. 2018, 2019) Public Data Release 2 (PDR2), JHK_s/K images from UltraVISTA Data Release 4 (DR4; McCracken et al. 2012) and UKIRT Infrared Deep Sky Survey (UKIDSS) UltraDeep Survey (UDS) Data Release 11 (DR11; Lawrence et al. 2007), and *Spitzer*/Infrared Array Camera (IRAC) [3.6] and [4.5] images from the *Spitzer* Large Area Survey with Hyper-Suprime-Cam (SPLASH). While all of our targets are not Lyman-break galaxies (LBGs) at $z > 13$ initially expected, they have collectively revealed an intriguing population of QGs in the intermediate-redshift range $z \sim 3$–4 as found by Harikane et al. (2024), which aligns with an alternative possibility suggested in Harikane et al. (2022). Despite this deviation from their initial expectation, we pursued a comprehensive study of these galaxies due to their significant scientific interest. As we noted later, these galaxies are found to be less massive ($\log_{10}(M_*/\mathrm{M}_\odot) < 10.3$) QGs found by using ground-based telescopes. The discussion based on spectroscopic observations regarding contamination and luminosity functions is presented in Harikane et al. (2024).

2.2 *JWST*/NIRSpec spectroscopy

This work uses *JWST*/NIRSpec data taken in a *JWST* program GO 1740 (PI: Y. Harikane). The NIRSpec spectra were taken in the fixed slit mode with S400A1 aperture, and the low-resolution ($R \sim$ 30–300) mode with PRISM/CLEAR covering the wavelength range of 0.60–5.3 μm. The spectra were obtained in the `2-POINT-NOD` mode with total exposure times are 2873 s for HD1, 1801 s for HD2, and 5041 s for HD3. These exposure times are adequate to detect the continuum and assess whether the galaxies are indeed LBGs or not.

We start from the level-2 data downloaded from the *Mikulski Archive for Space Telescopes* (*MAST*). We process the data using *JWST* pipeline version 1.14.0 with the Calibration Reference Data System (CRDS) pipeline mapping context 1229.

For HD3, we have observed flux losses in the *JWST*/NIRSpec spectrum compared to the *JWST*/NIRCam photometry. We have found that the spatial width of the aperture used in the 1D spectrum extraction process is about half the length of the spatial extent of its spectrum. Following advice from the *JWST* helpdesk, we re-extract the 1D spectrum of HD3 by default box car extraction method with a larger aperture enough to capture the whole spectrum. The spatial width of the aperture is defined based on a Gaussian fit to the spatial profile obtained by integrating the 2D spectrum over the wavelength direction.

2.3 *JWST*/NIRCam and *JWST*/MIRI imaging

Only for HD3, the NIRCam and MIRI images are available in the Public Release IMaging for Extragalactic Research (PRIMER, GO 1837, PI: J. S. Dunlop). We use the mosaic images of *F*090*W*, *F*115*W*, *F*150*W*, *F*200*W*, *F*277*W*, *F*356*W*, and *F*444*W* filters of the NIRCam instrument, as well as *F*770*W* and *F*1800*W* filters of the MIRI instrument, which were downloaded from the Dawn *JWST* Archive (DJA)[1] (mosaic version: v7.0) and reduced by GRIZLI (Brammer 2023). In Fig. 1, we show 4 arcsec × 4 arcsec cut-out images of HD3 for each available NIRCam and MIRI filters.

[1] https://dawn-cph.github.io/dja/

Downloaded from https://academic.oup.com/mnras/article/534/4/3552/7815198 by guest on 18 April 2025

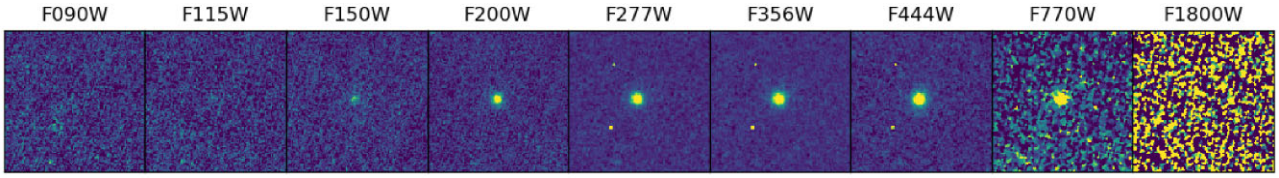

Figure 1. NIRCam and MIRI cut-out images of HD3. Each image measures 4 arcsec × 4 arcsec. Two bright dots seen in *F*277*W*, *F*356*W*, and *F*444*W* images are thought to be artefacts in images.

3 ANALYSES AND RESULTS

3.1 *JWST*/NIRSpec spectra for our targets

Our target spectra are presented in Fig. 2 that shows that the continuum breaks of the galaxies in the short wavelength are not as sharp as those that would be expected for Lyman break. Therefore, the *H*-band dropout is actually due to a Balmer break. For HD1, we find an emission line feature at 3.2 μm in the NIRSpec spectrum (see Fig. 2a). Given the redshift around 4 expected from the Balmer break wavelength, the emission line is likely to be blended H α + [N II], corresponding to the redshift $z = 4.0$. In the HD3 spectrum (Fig. 2c), there is an emission line feature at 2.8 μm. Given the redshift around 3 expected from the Balmer break, the emission line is likely to be blended H α + [N II], corresponding to the redshift $z = 3.2$. Another feature is observed at 2.1 μm, potentially corresponding to [O III], for the case of $z = 3.2$. We consider a negative signal at 4 μm to be caused by some error. We cannot find any significant line feature in the HD2 spectrum.

3.2 *JWST*/NIRCam and *JWST*/MIRI photometry of HD3

For HD3, we conduct aperture photometry by using PHOTUTILS 1.5.0 (Bradley et al. 2022) in available images of NIRCam and MIRI using a 0.3-arcsec-radius aperture, larger than the effective diameter $2R_e$ in the *F*200*W* image obtained by using GALFIT[2] (Peng et al. 2002, 2010a) as described in Section 3.5. The aperture radius is larger than the point spread function (PSF) full width at half-maximum (FWHM) size of all images except for *F*1800*W*. The photometric values with 1σ errors or 3σ upper limits are shown in Table 1. We estimate errors by performing aperture photometry randomly in the background region.

3.3 SED fitting

We conduct the spectral energy distribution (SED) fitting for the NIRSpec spectra. We employ the spectra spanning the range of 1.1–5.0 μm in our analysis, removing both short and long wavelengths where the uncertainty is large. We apply 2-pixel binning for the spectra to match the actual resolution of the data. We use the SED fitting code BAGPIPES[3] (Carnall et al. 2018) to perform SED fitting and estimate various physical parameters of the galaxies. The prior distributions employed in the fitting process can be found in Table 2. BAGPIPES relies on stellar population models from Bruzual & Charlot (2003), particularly the 2016 version from Chevallard & Charlot (2016), with initial mass function from Kroupa & Boily (2002). In our analysis, we incorporate the Calzetti model (Calzetti et al. 2000) to consider dust attenuation. Additionally, we adopt a delayed-τ star formation history (SFH) model with a form of the star formation rate (SFR) $\propto t \exp(-t/\tau)$.

We perform SED fitting in two approaches. Given the limited spectral resolution ($R \sim 100$) of our spectra and the fact that our targets are expected to be QGs without strong nebular emission lines, reliable fitting for metallicity and nebular parameters may be difficult. First, we perform the fitting with the metallicity value fixed at solar metallicity ($Z_*/Z_\odot = 1$), without nebular emission in our models. Second, we perform the fitting with the metallicity as a free parameter, still omitting nebular emission. In both cases, we conduct SED fitting by masking the line features.

For HD1, we set the redshift to $z = 4.0$, determined from the position of the potential H α + [N II] emission line. For HD3, we fix the redshift at $z = 3.20$ based on H α + [N II] emission line. However, for HD2, we define a redshift range from $z = 2.0$ to $z = 4.0$ based on the Balmer break position.

Table 3 provides the values of the derived posterior distributions. Figs 3, 4, and 5 display the fitting outcomes for each of our targets.

3.3.1 *HD1*

As mentioned in Section 3.1 (see also Fig. 2), the spectrum of HD1 exhibits a notable emission line identified as H α + [N II] emission. In order to minimize the influence of this emission line on the fitting process, we conduct SED fitting by masking the line as shown by the grey shade in the top panel of Fig. 3. Another point to note is that the photometric data points are not perfectly matched to the spectrum as found in the top panel of Fig. 3. Indeed, the photometric data of K_s, [3.6], and [4.5] show bluer colour than the spectrum. This discrepancy might be attributed to any systematic uncertainty of previous lower resolution and signal-to-noise ratio (S/N) photometric data. In this paper, we consider NIRSpec data to be more reliable than the photometric data.

As summarized in Table 3 and Fig. 3, the stellar mass of HD1 is $\log(M_*/\mathrm{M}_\odot) = 10.20^{+0.00}_{-0.01}$, a relatively modest value when compared to QGs typically observed with ground-based telescopes. The 3σ upper limit of SFR of HD1 is $\mathrm{SFR} < 0.12\,\mathrm{M}_\odot\,\mathrm{yr}^{-1}$. As a result, we find a specific star formation rate (sSFR) of $\log(\mathrm{sSFR}/\mathrm{yr}^{-1}) = -12.59^{+1.05}_{-3.02}$. This is consistent with a quiescent scenario because the sSFR value is more than 2 dex lower than that expected for the SFMS at redshift $z = 4$ as shown in Fig. 6. Other spectroscopically confirmed QGs at $z \simeq 4$ tend to be more massive, with $\log(M_*/\mathrm{M}_\odot) \gtrsim 10.3$ (Tanaka et al. 2019; Valentino et al. 2020; Antwi-Danso et al. 2023; Carnall et al. 2023b; Kakimoto et al. 2024). HD1 is the least massive QG observed at $z \simeq 4$ so far. We list the time of formation t_{form} and the time of quenching t_{quench} in Table 3, adopting the definitions by Carnall et al. (2018). The time

[2]https://users.obs.carnegiescience.edu/peng/work/galfit/galfit.html
[3]https://github.com/ACCarnall/bagpipes

Downloaded from https://academic.oup.com/mnras/article/534/4/3552/7815198 by guest on 18 April 2025

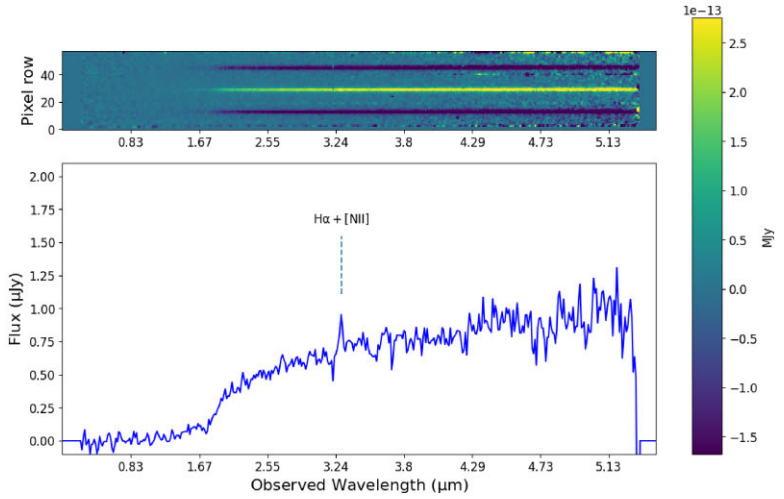

(a) HD1

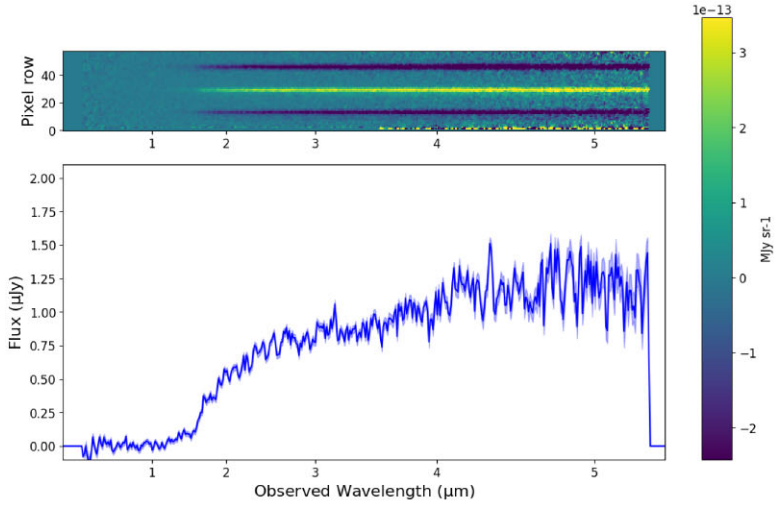

(b) HD2

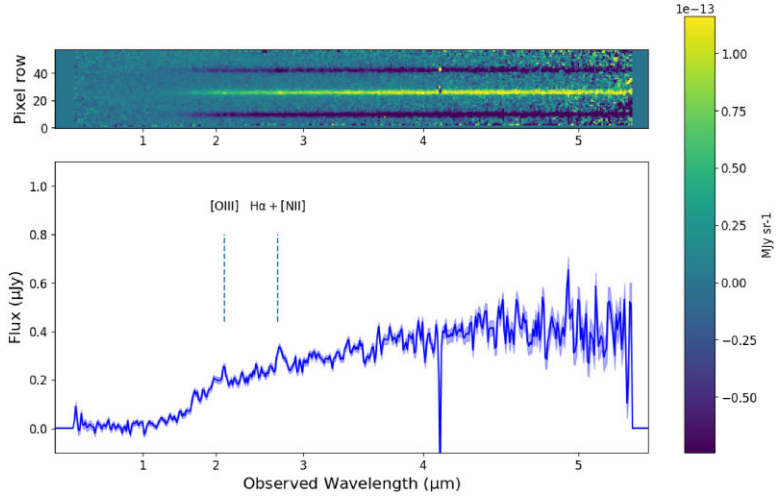

(c) HD3

Figure 2. 1D and 2D spectra of the target galaxies: (a) HD1, (b) HD2, and (c) HD3. Each figure consists of two panels: the top panel displays the 2D spectrum, where the horizontal axis denotes the observed wavelength (μm), and the vertical axis illustrates the spatial position along the slit (pixel). The colour bar shows flux density in the unit of MJy sr^{-1}. The bottom panel exhibits the 1D spectrum with the *x*-axis representing the observed wavelength (μm), and the *y*-axis representing the flux density (μJy). The blue line illustrates the observed flux, and the blue shaded region surrounding it represents the 1σ error region.

Downloaded from https://academic.oup.com/mnras/article/534/4/3552/7815198 by guest on 18 April 2025

Table 1. *JWST*/NIRCam and *JWST*/MIRI photometry of HD3. Flux densities or 3σ upper limits are shown in the unit of nJy.

ID	RA	Dec.	*JWST*/NIRCam							*JWST*/MIRI	
			F090W	*F115W*	*F150W*	*F200W*	*F277W*	*F356W*	*F444W*	*F770W*	*F1800W*
HD3	02:16:54.48	−05:09:37.1	< 55	< 44	97 ± 13	220 ± 13	328 ± 11	405 ± 10	486 ± 12	536 ± 42	< 457

Table 2. Free and pre-fixed physical parameters of SED fitting using BAGPIPES. The SED fitting is performed adopting a delayed τ SFH model and the Calzetti dust attenuation model.

Parameter	Value range
$\mathrm{Age_{del}}$ (Gyr)	(0.01, 2.0)
$\log_{10}(M_*/\mathrm{M}_\odot)$	(8.0, 12.0)
τ (Gyr)	(0.01, 2.0)
$Z_*/\mathrm{Z}_\odot$	1.0 (fixed)
A_V (mag)	(0.0, 4.0)
z	(2.0, 4.0)[a,b]

[a]For HD1, the redshift is fixed at $z = 4.0$ estimated from H α + [N II] emission line.
[b]For HD3, the redshift is fixed at $z = 3.2$ estimated from H α + [N II] emission line.

of formation t_{form} is defined as

$$t_{\mathrm{form}} = t(z_{\mathrm{form}}) = \frac{\int_0^{t_{\mathrm{obs}}} t\,\mathrm{SFR}(t)\,\mathrm{d}t}{\int_0^{t_{\mathrm{obs}}} \mathrm{SFR}(t)\,\mathrm{d}t}, \quad (1)$$

where $t_{\mathrm{obs}} = t(z_{\mathrm{obs}})$ is the age of the Universe at the redshift of observation z_{obs}.z_{form} corresponds to the redshift at which the stellar mass of the galaxy would have been half of its present mass. The time of quenching t_{quench} is the age of the Universe corresponding to the time where a normalized SFR becomes less than 10 per cent of averaged SFR across the history of the galaxy. The time-scale for quenching is defined as $\Delta t_{\mathrm{quench}} = t_{\mathrm{quench}} - t_{\mathrm{form}}$ (Carnall et al. 2018). It is approximately 0.3 Gyr. The mass-weighted age of HD1 is 0.72 Gyr. Corresponding redshifts for the formation and quenching times are $z_{\mathrm{form}} = 6.7$ and $z_{\mathrm{quench}} = 5.3$, respectively.

In the fitting with the free metallicity parameter, we also obtain a quiescent solution with a stellar mass of $\log(M_*/\mathrm{M}_\odot) = 10.23^{+0.02}_{-0.02}$. The stellar mass and the SFR are almost the same as those with the solar metallicity presented above. The metallicity is estimated as $0.08^{+0.03}_{-0.03}\,\mathrm{Z}_\odot$. Dust attenuation A_V is estimated to be higher ($A_V = 0.83$ mag) compared to when the metallicity is fixed at the solar value ($A_V = 0.25$ mag). This is because a bluer colour expected from the subsolar metallicity needs to be compensated by the higher dust attenuation. The mass-weighted age is slightly younger with a value of 0.63 Gyr.

3.3.2 HD2

In Fig. 4, on the contrary to HD1, the spectrum and photometry seem to match, except for the K band. Since the K-band photometric point is brighter, the photometric colour between K, [3.6], and [4.5] is bluer than the spectrum, mimicking an LBG solution. The stellar mass of HD2 is $\log(M_*/\mathrm{M}_\odot) = 10.16^{+0.00}_{-0.00}$ with a redshift of $z = 3.29$. HD2 exhibits the most significant quiescence because of the SFR $= 0.00\,\mathrm{M}_\odot\,\mathrm{yr}^{-1}$. We find $\log(\mathrm{sSFR/yr}^{-1}) = -15.72^{+2.26}_{-5.14}$, lowest value among our samples. This value is more than 2 dex lower than SFMS at $z = 3$ as shown in Fig. 6 and consistent with a quiescent scenario. The mass-weighted age of HD2 is 0.61 Gyr. The formation and quenching times listed in Table 3 correspond to the formation and quenching redshifts of $z_{\mathrm{form}} = 4.6$ and $z_{\mathrm{quench}} = 4.1$, respectively. The quenching time-scale $\Delta t_{\mathrm{quench}}$ is 0.2 Gyr.

In the fitting with the free metallicity parameter, we also obtain a quiescent solution with a stellar mass of $\log(M_*/\mathrm{M}_\odot) = 10.08^{+0.01}_{-0.00}$. The stellar mass and the SFR are almost same as the solar metallicity case. Redshift is estimated as $z = 3.17$. The metallicity is estimated as $2.05^{+0.05}_{-0.05}\,\mathrm{Z}_\odot$. Dust attenuation A_V is estimated to be lower ($A_V = 0.01$ mag) compared to when the metallicity is fixed at the solar value ($A_V = 0.44$ mag). An intrinsic redder colour expected from the higher metallicity needs less dust attenuation. The mass-weighted age is older with a value of 0.82 Gyr.

3.3.3 HD3

Rather than directly correcting the observed spectra using photometric data, we apply a photometric calibration to HD3 by including second-order Chebyshev polynomial terms in our fitting. In order to minimize the influence of this emission line on the fitting process, we conduct SED fitting by masking the line and artefact as shown by the grey shade in the top panel of Fig. 5. This calibration is performed considering only the available NIRCam photometry for HD3. As shown in the left middle panel of Fig. 5, the NIRCam photometric

Table 3. Physical properties of HD1, HD2, and HD3 obtained from SED fitting. SFR is the star formation rate and sSFR is specific star formation rate at the observed redshift. Values of SFR or 3σ upper limit of SFR are shown in this table. The age is defined as mass-weighted age. t_{form} and t_{quench} are defined as the age of the Universe corresponding to the time of formation and quenching, respectively.

ID	Age (Gyr)	$\log_{10}(M_*/\mathrm{M}_\odot)$	$\mathrm{SFR/M}_\odot\,\mathrm{yr}^{-1}$	$\log_{10}(\mathrm{sSFR/yr}^{-1})$	$Z/\mathrm{Z}_\odot$	A_V (mag)	t_{quench} (Gyr)	t_{form} (Gyr)	z
Fixed metallicity case									
HD1	$0.72^{+0.05}_{-0.03}$	$10.20^{+0.00}_{-0.01}$	< 0.12	$-12.59^{+1.05}_{-3.02}$	1	$0.25^{+0.04}_{-0.04}$	$1.07^{+0.07}_{-0.09}$	$0.79^{+0.03}_{-0.05}$	4.00
HD2	$0.61^{+0.03}_{-0.04}$	$10.16^{+0.00}_{-0.00}$	0.00	$-15.72^{+2.76}_{-5.14}$	1	$0.44^{+0.04}_{-0.02}$	$1.47^{+0.07}_{-0.07}$	$1.29^{+0.04}_{-0.03}$	$3.29^{+0.01}_{-0.01}$ [a]
HD3	$0.55^{+0.11}_{-0.09}$	$9.70^{+0.05}_{-0.05}$	$0.36^{+0.39}_{-0.29}$	$-10.16^{+0.30}_{-0.71}$	1	$0.35^{+0.25}_{-0.23}$	$1.89_{-0.14}$	$0.78^{+0.09}_{-0.11}$	3.20
Free metallicity case									
HD1	$0.63^{+0.03}_{-0.03}$	$10.23^{+0.02}_{-0.02}$	0.00	$-17.82^{+4.03}_{-6.76}$	$0.08^{+0.03}_{-0.03}$	$0.83^{+0.07}_{-0.07}$	$1.02^{+0.08}_{-0.06}$	$0.88^{+0.03}_{-0.03}$	4.00
HD2	$0.82^{+0.05}_{-0.06}$	$10.08^{+0.01}_{-0.00}$	< 0.03	$-18.02^{+4.35}_{-9.88}$	$2.05^{+0.05}_{-0.05}$	$0.01^{+0.01}_{-0.00}$	$1.35^{+0.10}_{-0.08}$	$1.17^{+0.04}_{-0.02}$	$3.17^{+0.01}_{-0.01}$ [a]
HD3	$0.68^{+0.09}_{-0.14}$	$9.66^{+0.05}_{-0.04}$	$0.05^{+0.31}_{-0.05}$	$-10.95^{+0.82}_{-2.43}$	$0.21^{+0.03}_{-0.02}$	$0.40^{+0.25}_{-0.20}$	$1.72^{+0.17}_{-0.20}$	$1.29^{+0.14}_{-0.02}$	3.20

[a]Systematic errors are adopted from Glazebrook et al. (2024).

Downloaded from https://academic.oup.com/mnras/article/534/4/3552/7815198 by guest on 18 April 2025

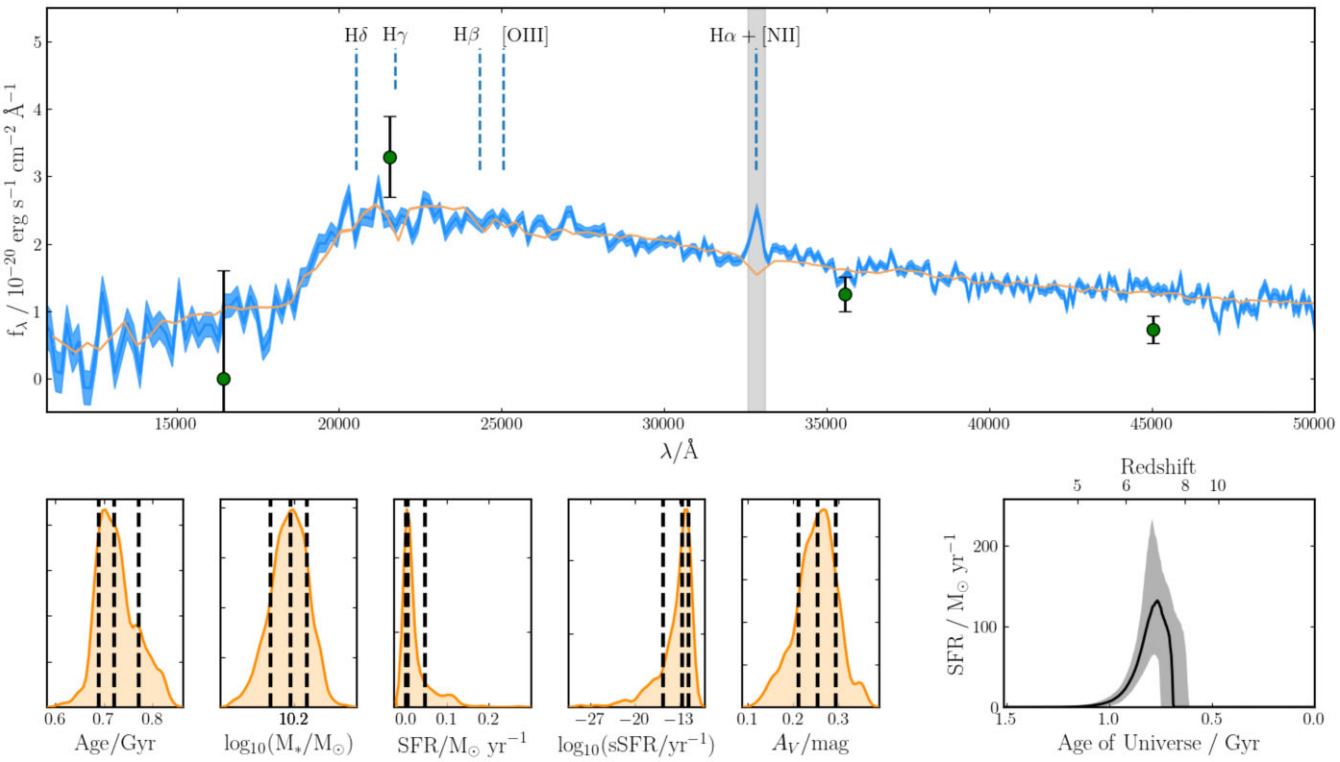

Figure 3. Fit result for HD1. In the top panel, the blue line corresponds to the observed spectrum data without binning, whereas the orange line represents the best-fitting SED, and the green plots represent photometric data points with 1σ error bars from Harikane et al. (2022), especially VISTA/H, K_s band, and *Spitzer*/IRAC [3.6] and [4.5]. Light grey shaded region represents a masked region that is not used in this fitting. The bottom-left five panels show the probability distributions of the parameters. The dashed lines correspond to the posterior percentiles of the 16th, 50th, and 84th. The bottom-right panel illustrates the SFH, featuring the median posterior of the best-fitting SFH depicted by the black line. The grey shaded region represents the 14th–68th percentile posterior distribution from the best-fitting SFH.

data and the model spectrum are in good agreement with each other after systematic correction by the second-order Chebyshev polynomial function in BAGPIPES, except for $F150W$ which is also consistent within a $\sim 2\sigma$ range. Based on the information provided in Table 3 and Fig. 5, it is evident that HD3 stands out as the least massive galaxy (i.e. $M_* < 10^{10}\,M_\odot$) among the target galaxies with the stellar mass of $\log(M_*/M_\odot) = 9.70^{+0.05}_{-0.05}$. HD3 has an SFR $= 0.36^{+0.39}_{-0.29}\,M_\odot\,\mathrm{yr}^{-1}$ and an sSFR of $\log(\mathrm{sSFR/yr}^{-1}) = -10.16^{+0.30}_{-0.71}$. This value is more than 2 dex lower than SFMS at $z = 3$ as shown in Fig. 6 and consistent with a quiescent/post-starburst scenario. The mass-weighted age of HD3 is 0.55 Gyr. The formation and quenching times in Table 3 correspond to the formation and quenching redshifts of $z_{\mathrm{form}} = 4.2$ and $z_{\mathrm{quench}} = 3.3$, respectively. The quenching time-scale $\Delta t_{\mathrm{quench}}$ is 0.4 Gyr.

In the fitting with the free metallicity parameter, we also obtain a quiescent solution with a stellar mass of $\log(M_*/M_\odot) = 9.66^{+0.05}_{-0.04}$. The stellar mass and the SFR are almost the same as those obtained with the solar metallicity. The metallicity is estimated as $0.21^{+0.03}_{-0.02}\,Z_\odot$. Dust attenuation A_V is estimated to be slightly higher ($A_V = 0.40$ mag) compared to the solar metallicity case ($A_V = 0.35$ mag) to compensate for a bluer intrinsic colour from the subsolar metallicity. The mass-weighted age is older with a value of 0.68 Gyr.

3.4 Emission line features of HD1 and HD3

Utilizing SPECUTILS (Earl et al. 2023), we quantify the line flux and the rest-frame equivalent width (EW) of the emission line features of HD1 and HD3 as summarized in Table 4.

We fit the line features by a single Gaussian profile to estimate the FWHM. The line fluxes are calculated by integrating the flux at the peak of the line feature over a width of two FWHM. EWs are also estimated over the same range as the line fluxes. The uncertainties are estimated as the standard deviations of the distributions of fluxes or EWs repeatedly measured at some random wavelength positions in each spectrum.

We find an emission line that seems to be the H α + [N II] emission line in the HD1 spectrum (see Fig. 3). We fit the line and have an FWHM of 2600 km s^{-1}, which is almost as same as the spectral resolution at the observed wavelength, indicating that the line is not resolved in this observation. The wavelength integration width is always set as 5 pixels, which is approximately twice the FWHM for this line.

We also find emission line features that seem to be the H α + [N II] and H β + [O III] emission line in the HD3 spectrum (see Fig. 5). For H α + [N II] emission line feature, we fit the line and have an FWHM of 6600 km s^{-1}. The spectral resolution at the observed wavelength is 3600 km s^{-1} indicating that the line is resolved. The wavelength integration width is always set as 8 pixels, which is approximately twice the FWHM for this line. For the [O III] emission line feature, we consider it to be the [O III] λλ4959, 5007 lines based on the position of H β, which is out of range from this feature. For this feature, we fit the line and have an FWHM of 3600 km s^{-1}. The spectral resolution at the observed wavelength is 5700 km s^{-1} indicating that the line remains unresolved. The wavelength integration width is always set as 4 pixels, which is approximately twice the FWHM for this line.

Downloaded from https://academic.oup.com/mnras/article/534/4/3552/7815198 by guest on 18 April 2025

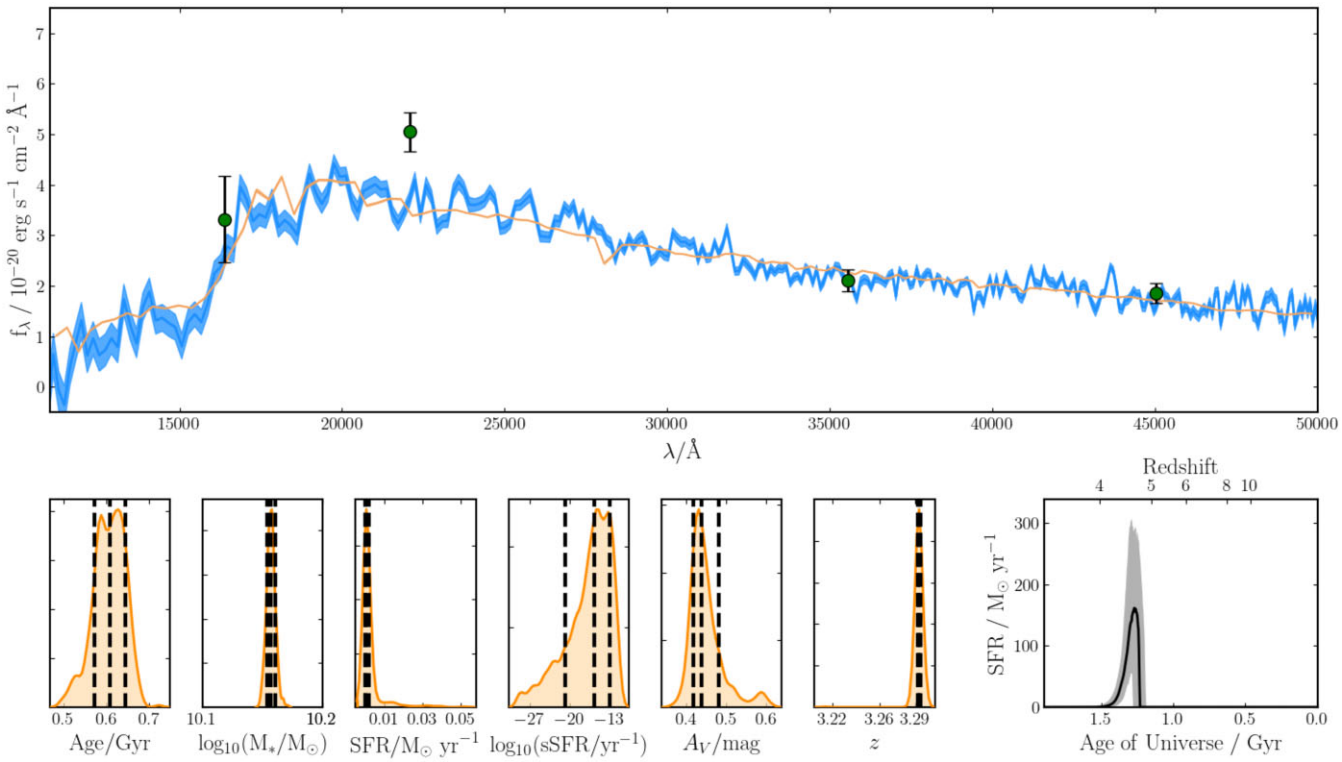

Figure 4. Same as Fig. 3, but for HD2, where the redshift is another free parameter. H, K-band data are from the United Kingdom Infrared Telescope (UKIRT).

In our spectra of HD1 and HD3, we plot the lines at the expected positions of H β, H γ, and H δ for reference. However, these lines have low significance in our spectra, so we do not analyse them in this paper.

3.5 Morphology of HD3

Since we have high spatial resolution NIRCam images of HD3, we examine the morphological features of HD3 using GALFIT (Peng et al. 2002, 2010a), a 2D profile fitting code. In this fitting procedure, we use a PSF generated by the stacking of stars in the same image. Generally, the galaxy size depends on the observed wavelength at $z < 3$ (e.g. van der Wel et al. 2014). To ensure consistency with the rest-frame wavelength in van der Wel et al. (2014), we assessed the morphology in the $F150W$, $F200W$, $F277W$, and $F356W$ images. We fit HD3 with a single Sérsic profile with free parameters: position, Sérsic index, effective radius, total magnitude, axis ratio, and position angle. The resulting morphological parameters for the images are outlined in Table 5. The effective radius $R_{e,F200W}$ is approximately 0.96 kpc (∼0.13 arcsec) and is sufficiently larger than empirical PSF FWHM size (0.1 arcsec), meaning HD3 is resolved. Sérsic index is estimated to be $n \simeq 1$, suggesting that HD3 shows a disc-like morphology.

Interestingly, the effective radius becomes smaller in longer wavelengths. This declining trend of size regarding the wavelength seen in some studies (e.g. van der Wel et al. 2014; Ito et al. 2024). Moreover, Sérsic index becomes larger at longer wavelengths. These trends might be related to the spatial distribution of past star formation within the galaxy. Since longer wavelengths trace older stellar populations, more centrally concentrated brightness profiles in longer wavelengths suggest such a distribution of older stellar populations, indicating the inside-out formation process (e.g. Nelson et al. 2012, 2016).

4 DISCUSSION

4.1 Origin of emission lines in HD1 and HD3 spectra

In this section, we discuss the possible origin of the H α + [N II] emission line feature seen in HD1 and HD3 spectra. An important thing to note is that we cannot estimate [N II]/H α from our data, but there are two possibilities that this line is H α dominant or [N II] dominant.

First, we discuss the possibilities of H α dominant case. In this case, there are two possibilities that the H α line is from AGN or star formation.

QGs exhibiting H α emission lines were identified by Carnall et al. (2023b, 2024), Nanayakkara et al. (2024), and de Graaff et al. (2024). In Nanayakkara et al. (2024), one QG displays prominent emission lines, suggesting the possibility of AGN activity. Moreover, seven other QGs show [O III] λ5007 or H β emission lines with S/N > 3, and four QGs show blended H α + [N II] emission lines. In Carnall et al. (2023b), H α and [N II] emission lines, as well as a marginal [O III] emission line, were observed in a QG at $z = 4.658$, with a clear broad H α component. The comparison of the strength of the H α narrow component with [N II] also indicates the presence of an AGN. Based on these findings, we consider the possibility of AGNs existing in our samples.

Assuming that most of the H α flux comes from a broad-line region of the AGN, we can estimate the black hole mass using the following formula in Greene & Ho (2005):

$$M_{\rm BH} = 2.0 \times 10^6 \times \left(\frac{L_{\rm H\alpha}}{10^{42}\ {\rm erg\ s^{-1}}}\right)^{0.55} \left(\frac{\rm FWHM_{H\alpha}}{10^3\ {\rm km\ s^{-1}}}\right)^{2.06} {\rm M_\odot}. \quad (2)$$

Downloaded from https://academic.oup.com/mnras/article/534/4/3552/7815198 by guest on 18 April 2025

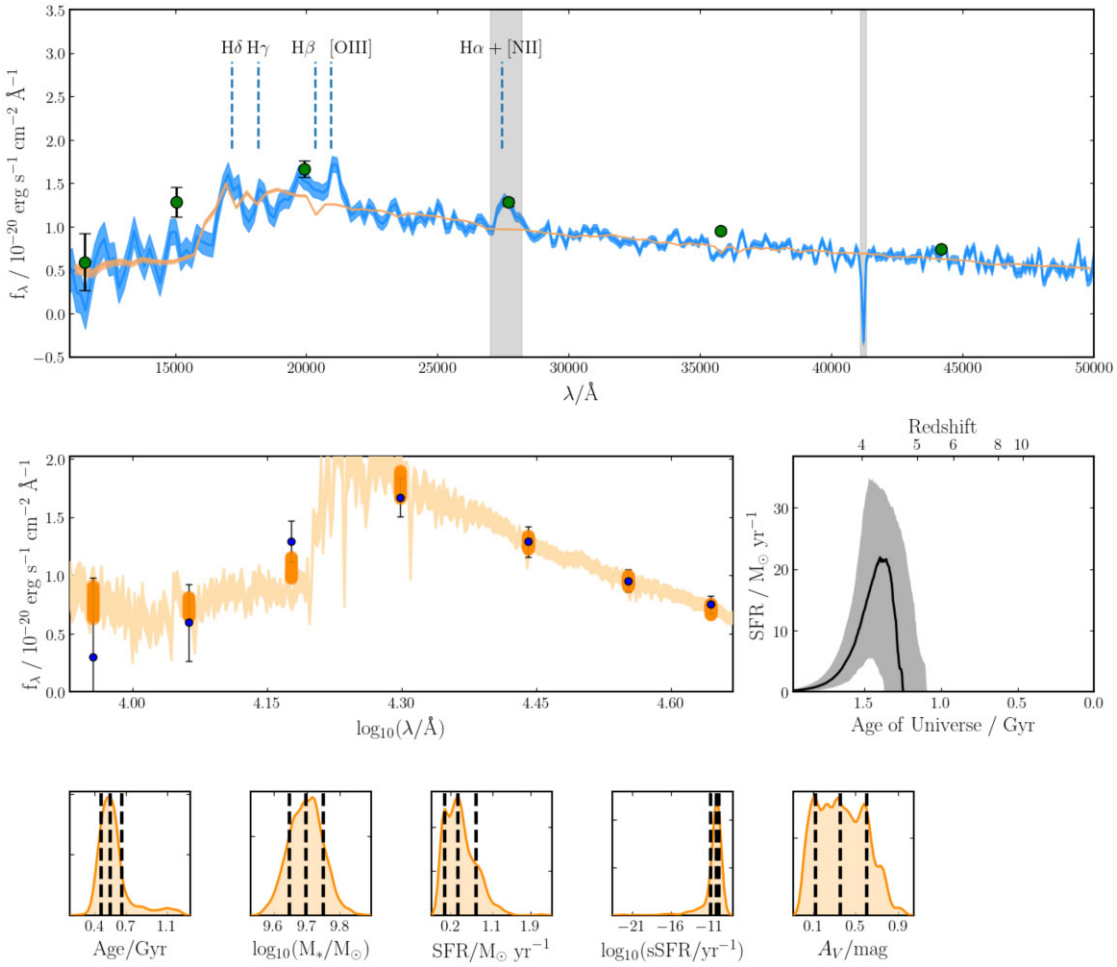

Figure 5. Same as Fig. 3, but for HD3. The photometric data in the top panel are our measurements based on NIRCam images (Table 1). The orange line is the best-fitting SED without calibration correction (see text). The middle left panel indicates the 16th–84th percentile posterior distribution from the best-fitting SED.

For HD1, we have an upper limit value of $\log(M_{\rm BH}/M_\odot) \simeq 6$ where FWHM of Hα + [N II] line is estimated as 2800 km s^{-1} from single Gaussian fitting. This FWHM is almost the same as the wavelength resolution in the spectrum around this wavelength range ≃2500 km s^{-1}, making our estimation an upper limit of the $M_{\rm BH}$. Some studies (de Graaff et al. 2024; Glazebrook et al. 2024; Nanayakkara et al. 2024) report that the spectral resolution of NIRSpec observation for objects that are much smaller than the slit width can be higher than the values presented by the Space Telescope Science Institute (STScI).[4] Although, we cannot measure the size of HD1, but if this is applicable to our targets, this emission might be resolved. For HD3, we have an upper limit value of $\log(M_{\rm BH}/M_\odot) \simeq 7$, where FWHM of H$\alpha$ + [N II] line was estimated as 7500 km s^{-1} from single Gaussian fitting. This FWHM is larger than the spectral resolution in the spectrum around this wavelength range ≃3500 km s^{-1}, indicating the presence of a broad Hα component. However, since the contribution of [N II] is unclear, it remains an upper limit. Although our estimated values are consistent with some faint AGNs, there are differences between these *JWST*-discovered faint AGNs (see e.g. Harikane et al. 2023; Maiolino et al. 2023) and our target galaxies, HD1 and HD3. Potential Hα broad-line fluxes in our work are notably lower, approximately 1 dex lower than Hα broad-line flux of faint AGNs found by *JWST* in previous studies. Therefore, if HD1 and HD3 host AGNs, they must be very faint AGNs. This might explain the lack of other emission lines in HD1, but it is challenging to conclude definitively from our result.

If we assume the line to be Hα + [N II] from star-forming regions, we can derive the SFR by using the conversion factor of Kennicutt (1998) and a [N II]/Hα ratio of ∼1/3 around the solar metallicity (e.g. Maiolino & Mannucci 2019). For HD1, $\rm SFR_{H\alpha} \sim 0.4\,M_\odot\,yr^{-1}$ after the dust correction based on A_V from the SED fitting and the Calzetti law (Calzetti et al. 2000). It is higher than the upper limit value of SFR derived from BAGPIPES; however, it is still consistent with a quiescent scenario. For HD3, the observed $\rm SFR_{H\alpha}$ is approximately $0.5\,M_\odot\,yr^{-1}$, which is higher than $\rm SFR_{BAGPIPES} = 0.1\,M_\odot\,yr^{-1}$. Although it exceeds the 2 dex lower bound of SFMS, it remains consistent with a quiescent scenario. These Hα emissions might result from present star formation. Additionally, it might indicate 'rejuvenation' (e.g. Thomas et al. 2010) where a galaxy experiences renewed star formation despite previous quiescent periods. Further investigation and analysis are essential to discern the true nature of this intriguing observation.

[4] https://jwst-docs.stsci.edu/jwst-near-infrared-spectrograph/nirspec-instrumentation/nirspec-dispersers-and-filters

Downloaded from https://academic.oup.com/mnras/article/534/4/3552/7815198 by guest on 18 April 2025

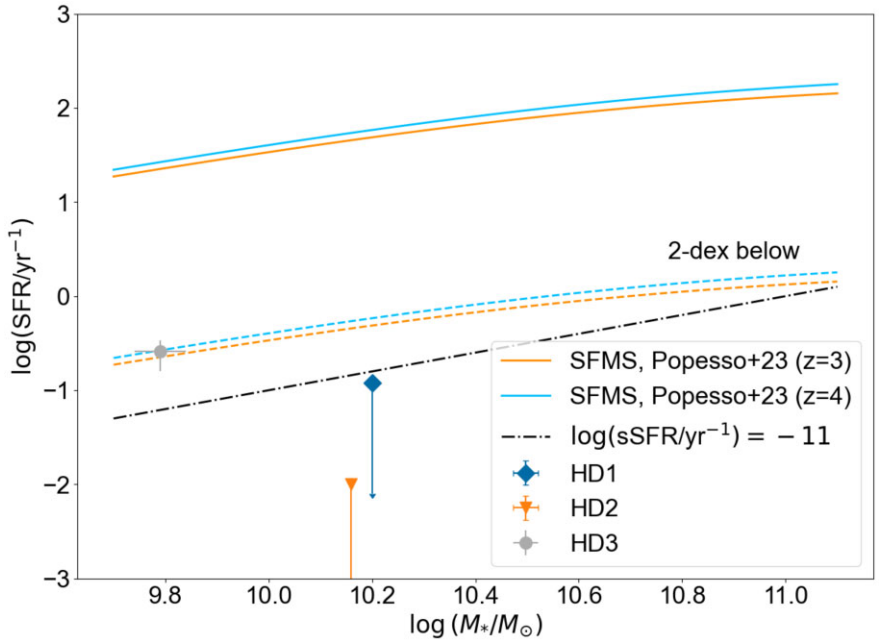

Figure 6. The SFR versus M_* of the target galaxies. The orange and blue lines represent the SFMS at redshifts $z = 3$ and $z = 4$, respectively, as derived from equation (14) in Popesso et al. (2023). Dashed lines indicate 2 dex below the SFMS, with each colour corresponding to the respective redshifts. The black dashed–dotted line denotes the threshold at $\log(\mathrm{sSFR}/\mathrm{yr}^{-1}) = -11$.

Table 4. Line flux and rest-frame EW of emission line features in the HD1 and HD3 spectra.

ID	Line	Flux (10^{-20} erg cm^{-2} s^{-1})	EW$_0$ (Å)
HD1	Hα + [N II]	44 ± 8	24 ± 4
HD3	Hα + [N II]	59 ± 11	61 ± 12
	[O III]	47 ± 6	37 ± 6

Table 5. Morphological parameters of HD3 obtained from GALFIT. R_e, n, and q denote the derived effective radius, Sérsic index, and axis ratio, respectively.

Filter	R_e (kpc)	n
F150W	0.948 ± 0.102	1.09 ± 0.18
F200W	0.959 ± 0.036	1.07 ± 0.07
F277W	0.797 ± 0.021	1.06 ± 0.11
F356W	0.687 ± 0.027	1.63 ± 0.20
F444W	0.648 ± 0.021	1.79 ± 0.17

Secondly, we discuss about possibilities of a [N II] dominant case. Recently, a $z = 2.445$ QG with an estimated stellar mass of $\log(M_*/\mathrm{M}_\odot) = 10.9$ was discovered by Belli et al. (2024). They detected both [N II] and [O III] emission lines in this QG. Based on the observed high [N II]/Hα and [O III]/Hβ line ratios, they provided a piece of compelling evidence for the presence of an AGN within the galaxy. Furthermore, their conclusions suggested that the AGN may have played a pivotal role in the quenching mechanism by expelling gas from the galaxy. In contrast, our observations of galaxy HD1 do not reveal Hβ or [O III] emission lines, nor do they show any absorption lines of Ca II K and Na I D, which were observed in the target of Belli et al. (2024). The estimated Hα + [N II] fluxes for HD1 and HD3 are notably weaker, approximately 2 dex lower than the [N II] flux observed in the galaxy studied by Belli et al. (2024). Note that the stellar masses of our targets are 0.5–1 dex lower than the QG in Belli et al. (2024). It is challenging to definitively determine whether this line is not an [N II] emission line or if the [O III] lines are genuinely absent.

HD3 exhibits a potential [O III] emission line feature, supporting the notion that HD3 has an AGN. However, the low resolution of our data prevents us from drawing definitive conclusions.

Certainly, there is a possibility that these Hα + [N II] emission lines may result from a complex combination of these cases.

4.2 Size–mass relation

The size–mass relation, describing the relationship between the effective radius and stellar mass of galaxies, is pivotal for comprehending their formation and evolution across cosmic time. Studying this relation across various galaxy populations, such as QGs and SFGs, enables us to discern differences in their evolutionary pathways.

Fig. 7 shows the size–mass relation from some studies, including QGs and SFGs at $z \sim 0.75$ and $z \sim 2.75$ from van der Wel et al. (2014), QGs at $z = 0.6$–0.8 and $z = 1.0$–1.3 from Hamadouche et al. (2022), and QGs at $z = 1.0$–1.5 and $z = 1.5$–2.0 from Nedkova et al. (2021), and *UVJ*-selected QGs at $z \geq 3$ from Ito et al. (2024). The relations from van der Wel et al. (2014), Hamadouche et al. (2022), and Ito et al. (2024) are extrapolated for stellar masses below $10^{10.3}$ M$_\odot$. This is because the data used to establish the size–mass relations in van der Wel et al. (2014) only considered galaxies with masses exceeding $10^{10.3}$ M$_\odot$, and the same criterion was followed in Hamadouche et al. (2022) and Ito et al. (2024). It also depicts the sizes and masses of individual *UVJ*-selected QGs from Ito et al. (2024), as well as a QG at $z = 4.658$ from Carnall et al. (2023b), SXDS-27434 ($z = 4.01$) reported in Tanaka et al. (2019) and Valentino et al. (2020), and HD3.

In Fig. 7, HD3 occupies a position between what is typically observed for QGs and SFGs at $z = 2.75$ as reported by van der Wel et al. (2014). Furthermore, HD3 falls above the extrapolated size–mass relation proposed by Ito et al. (2024). However, there

Downloaded from https://academic.oup.com/mnras/article/534/4/3552/7815198 by guest on 18 April 2025

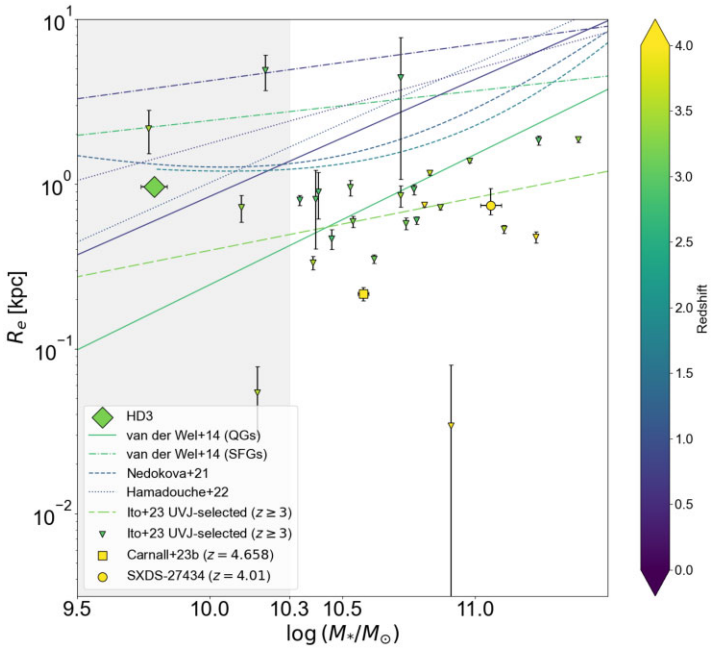

Figure 7. Size–mass relation and HD3. Each line shows the size–mass relation of galaxies. Ito et al. (2024) in long-dashed line (UVJ-selected). van der Wel et al. (2014) in solid and dashed–dotted lines. Nedkova et al. (2021) in dashed lines. Hamadouche et al. (2022) in dotted lines. The data used to establish the size–mass relations in van der Wel et al. (2014) only considered galaxies with masses exceeding $10^{10.3}$ $M_\odot$, and the same criterion was followed in Hamadouche et al. (2022) and Ito et al. (2024). The region corresponds to $M_* < 10^{10.3}$ $M_\odot$ shown in grey shaded region. Markers show sizes and masses of individual QGs from Ito et al. (2024) and Carnall et al. (2023b) and SXDS-27434 (see Tanaka et al. 2019; Valentino et al. 2020; Ito et al. 2024). The colours of the symbols and lines indicate the redshift as shown in the colour bar.

is a larger scatter reported especially for the less massive regime of $\log(M_*/M_\odot) < 10.3$ (Cutler et al. 2024; Ito et al. 2024) within which HD3 falls. Additionally, some studies (e.g. Kawinwanichakij et al. 2021; Nedkova et al. 2021) have reported bending in the size–mass relation of $z > 2$ QGs at $\log(M_*/M_\odot) = 10$–10.5. This may explain HD3's position above the size–mass relation.

The Sérsic index of HD3 is 1.07 ± 0.07 as shown in Table 5. This value is similar to some QGs in Cutler et al. (2024) and Ito et al. (2024), which display disc-like features. Suggesting that HD3 is currently undergoing a phase of morphological transition, akin to what Cutler et al. (2024) and Ito et al. (2024) pointed out for their disc-like QG samples. Ito et al. (2024) characterized a disc fraction of QGs, which is defined as the fraction of disc-like galaxies having the $F277W$ Sérsic index below 2. They found a higher disc fraction of QGs in samples at $z > 3.3$ compared to those at $z < 3.3$. Cutler et al. (2024) also indicate less massive QG candidates tend to have disc-like profiles based on photometric selected samples.

QGs show a steeper size–mass relation compared to SFGs in previous studies (e.g. van der Wel et al. 2014). High-redshift massive QGs are more compact and highly dense within their effective radius compared with their local counterparts. This alignment with inside-out growth scenarios, where minor mergers are implicated as origin, is supported by observations (e.g. Bezanson et al. 2009; van Dokkum et al. 2010, 2015; Cimatti, Nipoti & Cassata 2012) and simulations (e.g. Naab et al. 2009; Hilz, Naab & Ostriker 2013; Hopkins et al. 2013). Hamadouche et al. (2022) reported that the size evolution of massive QGs from $z = 1.1$ to $z = 0.7$ might be dominated by minor mergers rather than major mergers. These minor mergers tend to make the galaxy radius larger, but the stellar mass does not evolve significantly when compared with major mergers, causing the size–mass relation to be steeper for QGs. However, HD3 is not showing elliptical in Sérsic profile and likely represents a disc population ($n = 1$) with stellar mass lower than $\log(M_*/M_\odot) = 10$. Cutler et al. (2024) reported a difference between the size–mass relation in less massive QG candidates and massive QG candidates, divided by $\log(M_*/M_\odot) = 10.3$. Cutler et al. (2024) also found that massive QGs primarily evolve through mass quenching mechanisms, whereas less massive QGs are affected by other processes like environmental or feedback-driven quenching. Our findings support these variations in the mechanisms driving the evolution of galaxy size between massive QGs and less massive QGs.

4.3 Implications for quiescent galaxy quenching mechanism

Considering quenching mechanisms, the time-scale is an important factor to distinguish how QGs are quenched. There are roughly two types of quenching: 'fast' and 'slow' time-scale quenching (e.g. Carnall et al. 2018; Belli, Newman & Ellis 2019). From the result of SED fitting, we have quenching time-scales of $\simeq$0.2–0.7 Gyr for these galaxies, which are categorized as fast quenching. These values are consistent with quenching time-scales for high-redshift QGs. Carnall et al. (2018) concluded that rapid quenching with < 1 Gyr might be the result of quasar-mode AGN feedback. In some simulations, AGN feedback is shown to contribute to rapid quenching. Weller et al. (2024) used the cosmological simulations `IllustrisTNG` and `ASTRID`, measuring typical quenching time-scales of approximately ∼200–600 Myr for these two simulations. In both simulations, AGN feedback plays a crucial role in quenching star formation. However, in `IllustrisTNG`, AGN kinetic feedback is the dominant mechanism driving rapid quenching, whereas in `ASTRID`, AGN thermal feedback is less effective, leading to a slightly longer quenching time-scale. Other simulations also conclude that AGN feedback plays a crucial role in quenching, but the mechanisms are complex and not solely dependent on AGN feedback

Downloaded from https://academic.oup.com/mnras/article/534/4/3552/7815198 by guest on 18 April 2025

(e.g. Kimmig et al. 2023; Remus & Kimmig 2023). Combined with our discussion in Section 4.1 that HD1 and HD3 might host AGN, our target galaxies might be quenched by AGN feedback.

It is also worth noting that we do not detect any companion galaxies in close proximity within a radius of 15 arcsec and redshift ranges 3.05–3.35 to HD3 in the *JWST*/PRIMER-UDS photo-z catalogue provided by DJA and Cosmic Assembly Near-infrared Deep Extragalactic Legacy Survey (CANDELS; Grogin et al. 2011; Koekemoer et al. 2011). HD1 and HD2 are positioned out of the area of CANDELS (Grogin et al. 2011; Koekemoer et al. 2011) COSMOS/UDS photometric redshift catalogue (Kodra et al. 2023), indicating the need for further research of the environment around these objects. This observation raises questions about the QG formation scenario driven by environmental factors, as this scenario is often proposed for less massive QGs. In the local Universe, low-mass QGs are believed to be quenched by environmental effects (Roberts et al. 2019; Contini et al. 2020). Pasha et al. (2023) noted that dwarf galaxies at $2 < z < 5$ with stellar masses ranging from $\log(M_*/\mathrm{M}_\odot) = 5.5$ to 8.5 are quenched by environmental effects such as shock heating from cosmic sheets and filaments, but given HD3's larger stellar mass, the influence of environmental effects remains uncertain.

It is important to note that the low dispersion of our current data and the absence of visible absorption lines prevent us from ruling out the possibility that the cessation of star formation may be temporary due to strong supernova feedback.

4.4 Role of high-redshift intermediate-mass QGs in galaxy formation and evolution

Our result raises the possibility of the existence of AGNs in some QGs with a stellar mass range of $\log(M_*/\mathrm{M}_\odot) < 11$. If this is the case, the progenitors of these galaxies might be explained by low-mass AGNs at higher redshift. In recent studies using *JWST*, an unexpectedly large number of faint AGNs are found at $z \gtrsim 4$ (e.g. Harikane et al. 2023; Maiolino et al. 2023). In Suh et al. (2024), a possible low-mass BH has been found at $z \sim 4$. Studying intermediate-mass QGs might help our understanding of the descendants of these faint AGNs. By studying intermediate-mass QGs, we might be able to understand the relation between quenching and faint AGNs.

Weibel et al. (2024) recently found a QG at $z \sim 7$ with similar stellar mass of our galaxies $\log(M_*/\mathrm{M}_\odot) \sim 10.2$. Our galaxies, particularly HD1, may represent a similar type of QG, formed slightly later. Additionally, a post-starburst galaxy at $z \sim 5$ (Strait et al. 2023) and a mini-quenched galaxy at $z \sim 7$ (Looser et al. 2024) have also been recently discovered by *JWST*. We need more samples to discuss the relations of QGs at higher redshifts $z > 4$ with those at intermediate redshifts $z \lesssim 4$.

The intermediate-mass regime is another key feature of our sample, which is essential for determining which quenching mechanism is dominant depending on the stellar mass. Additionally, this regime helps clarify the role and position of QGs in the galaxy formation and evolution pathways, as well as their contribution to reionization and star formation across cosmic history.

5 CONCLUSIONS

In this paper, we analyse the *JWST*/NIRSpec spectrum of three galaxies HD1, HD2, and HD3 identified during the pre-*JWST*. Using BAGPIPES SED fitting code, together with available *JWST*/NIRCam photometry of HD3, we derive some physical parameters for these galaxies.

Our major findings in this fitting are as follows.

(i) For HD1, we find redshift $z = 4.00$ from the position of the potentially blended Hα + [N II] line in its spectrum. HD1 is the least massive QGs spectroscopically observed around $z = 4$ with a stellar mass of $\log(M_*/\mathrm{M}_\odot) = 10.20$. The SFR of HD1 is $\mathrm{SFR}/\mathrm{M}_\odot\,\mathrm{yr}^{-1} < 0.12$ which aligns with a quiescent scenario.

(ii) HD2 is a less massive QG at $z = 3.29$ with a stellar mass of $\log(M_*/\mathrm{M}_\odot) = 10.16$. The SFR of HD2 is $\mathrm{SFR}/\mathrm{M}_\odot\,\mathrm{yr}^{-1} = 0.00$ which aligns with a quiescent scenario.

(iii) HD3 is the least massive QG in our targets at $z = 3.20$ with a stellar mass of $\log(M_*/\mathrm{M}_\odot) = 9.70$. The SFR of HD3 is $\mathrm{SFR}/\mathrm{M}_\odot\,\mathrm{yr}^{-1} = 0.36$ which aligns with a quiescent scenario.

Two of the target galaxies, HD1 and HD3, exhibit a potential Hα + [N II] emission line within their spectra. We discuss the possible origins of these emission lines. One possibility is that they are Hα-dominant emission lines from AGN (e.g. Carnall et al. 2023b) within these galaxies or instantaneous star formation events like rejuvenation. Another possibility is that they are [N II]-dominant emission lines from AGN (e.g. Belli et al. 2024) or a combination of these cases. Future high-resolution observations using *JWST*/NIRSpec or other instruments might provide more perspectives on this matter.

By using GALFIT 2D profile fitting code, we study the morphology of HD3 in NIRCam images. HD3 exhibits a disc-like morphology with Sérsic index $n \simeq 1$. From this result, HD3 may be undergoing a phase of morphological transformation. HD3 has a larger effective radius expected by extrapolated size–mass relation of $z \sim 3$ QGs in van der Wel et al. (2014) and Ito et al. (2024) This result is consistent with flatten of size–mass relation of QGs in less massive end reported in Kawinwanichakij et al. (2021) and Nedkova et al. (2021). This might be a result of a difference in size evolution pathways between high-mass QGs and low-mass QGs (e.g. van Dokkum et al. 2015; Cutler et al. 2024).

Recent observations with *JWST* (Carnall et al. 2023b; Nanayakkara et al. 2024) and simulations (Hartley et al. 2023; Bluck et al. 2024) suggest that AGNs are the most likely progenitors for the quenching of massive QGs ($\log(M_*/\mathrm{M}_\odot) > 10$) at $z > 3$. However, for low-mass QGs ($\log(M_*/\mathrm{M}_\odot) < 9$), environmental quenching is considered a possible mechanism. None the less, the quenching mechanisms of high-redshift QGs with stellar masses around $\log(M_*/\mathrm{M}_\odot) \simeq 9$–10 remain uncertain. The short quenching time-scales of our targets, ranging from 0.2 to 0.7 Gyr, suggest that these galaxies might be quenched by strong AGN feedback (Carnall et al. 2018), combined with the possible presence of AGN indicated from Hα + [N II] emission line in HD1 and HD3. The lack of detected companion galaxies in close proximity to HD3 challenges the prevailing idea that environmental factors drive the formation of QGs, particularly for less massive ones with stellar masses of $\sim \log(M_*/\mathrm{M}_\odot) = 10$. If AGNs exist in our targets, the possibility of AGN-driven quenching in the intermediate-mass range of $\log(M_*/\mathrm{M}_\odot) \simeq 9$–10 becomes more plausible. Future deep and high-resolution observations of our targets and other intermediate-mass QGs by NIRSpec and NIRCam or other instruments could be crucial in exploring the quenching mechanisms and understanding the galaxy formation and evolution pathway across cosmic history.

ACKNOWLEDGEMENTS

We are grateful for the useful discussion with Takumi Tanaka. We are also thankful for the valuable information regarding the NIRSpec

Downloaded from https://academic.oup.com/mnras/article/534/4/3552/7815198 by guest on 18 April 2025

data and for the support and expertise in NIRSpec and data reduction offered by the *JWST* helpdesk, especially Charles R. Proffitt, Tony Keyes, and Maria Pena-Guerrero.

We deeply thank the anonymous referee for constructive comments that improve the quality and clarity of this paper.

AKI was supported by JSPSKAKENHI grant number 23H00131. YT was supported by JSPSKAKENHI grant numbers 22H04939 and 23K20035. TH was supported by Leading Initiative for Excellent Young Researchers, MEXT, Japan (HJH02007) and by JSPSKAKENHI grant number 22H01258. KI was supported by JSPSKAKENHI grant numbers JP22J00495 and JP23K13141.

This work is based on observations made with the NASA/ESA/CSA *JWST*. The data were obtained from the *Mikulski Archive for Space Telescopes* (*MAST*) at the Space Telescope Science Institute (STScI), which is operated by the Association of Universities for Research in Astronomy, Inc., under NASA contract NAS 5–03127 for *JWST*. These observations are associated with program #1740. This paper used the data products retrieved from the Dawn *JWST* Archive (DJA). DJA is an initiative of the Cosmic Dawn Center, which is funded by the Danish National Research Foundation under grant number 140.

DATA AVAILABILITY

All NIRSpec data are available via the *Mikulski Archive for Space Telescopes* (*MAST*) (https://mast.stsci.edu). The BAGPIPES code is publicly available at https://github.com/ACCarnall/bagpipes. NIRCam and MIRI imaging data used in this paper are available in the Dawn *JWST* Archive (DJA) at https://dawn-cph.github.io/dja/.

REFERENCES

Aihara H. et al., 2018, PASJ, 70, S4
Aihara H. et al., 2019, PASJ, 71, 114
Alberts S. et al., 2023, preprint (arXiv:2312.12207)
Antwi-Danso J. et al., 2023, preprint (arXiv:2307.09590)
Belli S. et al., 2024, Nature, 630, 54
Belli S., Newman A. B., Ellis R. S., 2019, ApJ, 874, 17
Bezanson R., van Dokkum P. G., Tal T., Marchesini D., Kriek M., Franx M., Coppi P., 2009, ApJ, 697, 1290
Bluck A. F. L. et al., 2024, ApJ, 961, 163
Boselli A., Fossati M., Sun M., 2022, A&AR, 30, 3
Bradley L. et al., 2022, astropy/photutils: 1.5.0 (1.5.0). Zenodo (https://doi.org/10.5281/zenodo.6825092)
Brammer, G., 2023, grizli (1.9.11). Zenodo, https://doi.org/10.5281/zenodo.8370018
Brinchmann J., Charlot S., White S. D. M., Tremonti C., Kauffmann G., Heckman T., Brinkmann J., 2004, MNRAS, 351, 1151
Bruzual G., Charlot S., 2003, MNRAS, 344, 1000
Calzetti D., Armus L., Bohlin R. C., Kinney A. L., Koornneef J., Storchi-Bergmann T., 2000, ApJ, 533, 682
Carnall A. C. et al., 2023a, MNRAS, 520, 3974
Carnall A. C. et al., 2023b, Nature, 619, 716
Carnall A. C. et al., 2024, MNRAS, 534, 325
Carnall A. C., McLure R. J., Dunlop J. S., Davé R., 2018, MNRAS, 480, 4379
Chevallard J., Charlot S., 2016, MNRAS, 462, 1415
Cimatti A., Nipoti C., Cassata P., 2012, MNRAS, 422, L62
Contini E., Gu Q., Ge X., Rhee J., Yi S. K., Kang X., 2020, ApJ, 889, 156
Croton D. J. et al., 2006, MNRAS, 365, 11
Cutler S. E. et al., 2024, ApJ, 967, L23
D'Eugenio C. et al., 2021, A&A, 653, A32
Davidzon I. et al., 2017, A&A, 605, A70
de Graaff A. et al., 2024, preprint (arXiv:2404.05683)
Earl N. et al., 2023, astropy/specutils: v1.11.0. Zenodo (https://doi.org/10.5281/zenodo.8049033)
Forrest B. et al., 2020, ApJ, 890, L1
Furusawa H. et al., 2008, ApJS, 176, 1
Gabor J. M., Davé R., Finlator K., Oppenheimer B. D., 2010, MNRAS, 407, 749
Glazebrook K. et al., 2017, Nature, 544, 71
Glazebrook K. et al., 2024, Nature, 628, 277
Greene J. E., Ho L. C., 2005, ApJ, 630, 122
Grogin N. A. et al., 2011, ApJS, 197, 35
Hamadouche M. L. et al., 2022, MNRAS, 512, 1262
Harikane Y. et al., 2022, ApJ, 929, 1
Harikane Y. et al., 2023, ApJ, 959, 39
Harikane Y. et al., 2024, preprint (arXiv:2406.18352)
Hartley A. I. et al., 2023, MNRAS, 522, 3138
Hilz M., Naab T., Ostriker J. P., 2013, MNRAS, 429, 2924
Hopkins P. F., Cox T. J., Hernquist L., Narayanan D., Hayward C. C., Murray N., 2013, MNRAS, 430, 1901
Houston T., Croton D. J., Sinha M., 2023, MNRAS, 522, L11
Ito K. et al., 2024, ApJ, 964, 192
Kakimoto T. et al., 2024, ApJ, 963, 49
Kawinwanichakij L. et al., 2021, ApJ, 921, 38
Kennicutt R. C., Jr, 1998, ARA&A, 36, 189
Kimmig L. C., Remus R.-S., Seidel B., Valenzuela L. M., Dolag K., Burkert A., 2023, preprint (arXiv:2310.16085)
Kodra D. et al., 2023, ApJ, 942, 36
Koekemoer A. M. et al., 2011, ApJS, 197, 36
Kroupa P., Boily C. M., 2002, MNRAS, 336, 1188
Lawrence A. et al., 2007, MNRAS, 379, 1599
Looser T. J. et al., 2024, Nature, 629, 53
Maiolino R. et al., 2012, MNRAS, 425, L66
Maiolino R. et al., 2023, preprint (arXiv:2308.01230)
Maiolino R., Mannucci F., 2019, A&AR, 27, 3
Marchesini D. et al., 2023, ApJ, 942, L25
Martig M., Bournaud F., Teyssier R., Dekel A., 2009, ApJ, 707, 250
Mawatari K. et al., 2020, ApJ, 889, 137
Mawatari K., Yamada T., Fazio G. G., Huang J.-S., Ashby M. L. N., 2016, PASJ, 68, 46
McCracken H. J. et al., 2012, A&A, 544, A156
Merlin E. et al., 2019, MNRAS, 490, 3309
Naab T., Johansson P. H., Ostriker J. P., 2009, ApJ, 699, L178
Nanayakkara T. et al., 2024, Sci. Rep., 14, 3724
Nedkova K. V. et al., 2021, MNRAS, 506, 928
Nelson E. J. et al., 2012, ApJ, 747, L28
Nelson E. J. et al., 2016, ApJ, 828, 27
Newman A. B., Ellis R. S., Bundy K., Treu T., 2012, ApJ, 746, 162
Ownsworth J. R., Conselice C. J., Mortlock A., Hartley W. G., Almaini O., Duncan K., Mundy C. J., 2014, MNRAS, 445, 2198
Pasha I., Mandelker N., van den Bosch F. C., Springel V., van de Voort F., 2023, MNRAS, 520, 2692
Peng C. Y., Ho L. C., Impey C. D., Rix H.-W., 2002, AJ, 124, 266
Peng C. Y., Ho L. C., Impey C. D., Rix H.-W., 2010a, AJ, 139, 2097
Peng Y.-j. et al., 2010b, ApJ, 721, 193
Peng Y., Maiolino R., Cochrane R., 2015, Nature, 521, 192
Piotrowska J. M., Bluck A. F. L., Maiolino R., Peng Y., 2022, MNRAS, 512, 1052
Popesso P. et al., 2023, MNRAS, 519, 1526
Remus R.-S., Kimmig L. C., 2023, preprint (arXiv:2310.16089)
Roberts I. D., Parker L. C., Brown T., Joshi G. D., Hlavacek-Larrondo J., Wadsley J., 2019, ApJ, 873, 42
Sandles L. et al., 2023, preprint (arXiv:2307.08633)
Santini P. et al., 2017, ApJ, 847, 76
Santini P. et al., 2019, MNRAS, 486, 560
Schreiber C. et al., 2018a, A&A, 611, A22
Schreiber C. et al., 2018b, A&A, 618, A85
Scoville N. et al., 2007, ApJS, 172, 1
Somerville R. S., Davé R., 2015, ARA&A, 53, 51

Downloaded from https://academic.oup.com/mnras/article/534/4/3552/7815198 by guest on 18 April 2025

Speagle J. S., Steinhardt C. L., Capak P. L., Silverman J. D., 2014, ApJS, 214, 15
Strait V. et al., 2023, ApJ, 949, L23
Suh H. et al., 2024, preprint (arXiv:2405.05333)
Tanaka M. et al., 2019, ApJ, 885, L34
Thomas D., Maraston C., Schawinski K., Sarzi M., Silk J., 2010, MNRAS, 404, 1775
Valentino F. et al., 2020, ApJ, 889, 93
Valentino F. et al., 2023, ApJ, 947, 20
van der Wel A. et al., 2014, ApJ, 788, 28
van Dokkum P. G. et al., 2010, ApJ, 709, 1018
van Dokkum P. G. et al., 2015, ApJ, 813, 23
Weibel A. et al., 2024, preprint (arXiv:2409.03829)
Weller E. J., Pacucci F., Ni Y., Hernquist L., Park M., 2024, preprint (arXiv:2406.02664)
Whitaker K. E. et al., 2014, ApJ, 795, 104
Whitaker K. E., van Dokkum P. G., Brammer G., Franx M., 2012, ApJ, 754, L29
Zolotov A. et al., 2015, MNRAS, 450, 2327

This paper has been typeset from a TEX/LATEX file prepared by the author.

Downloaded from https://academic.oup.com/mnras/article/534/4/3552/7815198 by guest on 18 April 2025

© 2024 The Author(s).
Published by Oxford University Press on behalf of Royal Astronomical Society. This is an Open Access article distributed under the terms of the Creative Commons Attribution License (https://creativecommons.org/licenses/by/4.0/), which permits unrestricted reuse, distribution, and reproduction in any medium, provided the original work is properly cited.